Journal of Thermal Science Vol.29, No.6 (2020) 1463−1474

https://doi.org/10.1007/s11630-020-1251-0 **Article ID: 1003-2169(2020)06-1463-12**

Experimental Investigation of the Secondary Flow in a Rotating Smooth Channel Subjected to Thermal Boundary Conditions

LI Haiwang, YOU Haoliang, YOU Ruquan*, TAO Zhi

National Key Laboratory of Science and Technology on Aero-Engines Aero-thermodynamics, Beihang University, Beijing 100191, China

Abstract: In the current study, thermal boundary conditions are considered in a rotating smooth channel with a square cross-section to investigate the secondary flow and compare it to that of the same channel without heating. The measurement is conducted at three streamwise planes (X=445 mm, 525 mm, 605 mm). The flow parameters are the Reynolds number (Re=4750, which was based on the average longitudinal or primary velocity U and the hydraulic diameter D of the channel cross-section), the rotation number ($Ro=\Omega D/U$, where Ω is the rotational velocity, ranging from 0 to 0.26), and the aspect ratio of the channel cross-section (AR=1, which is calculated by dividing the channel height by the channel width). The leading and trailing walls are heated under a constant heat flux q_w=380 W/m^2, and the top and bottom walls are isothermal at room temperature. This work is in a series with our previous work without thermal boundary conditions. Based on the experimental data, we obtained a four-vortex regime. There is a counter-rotating vortex pair near the leading side and the trailing side. Because the leading and trailing walls are heated, the buoyancy force increases the relative vertical position of the vortex pair near the trailing side from 5% to 12.5% of the hydraulic diameter. When moving upstream along the streamwise direction, the upper vortex near the trailing wall becomes weaker, whereas the lower vortex becomes stronger. As the rotational speed increases, the vortex pair near the trailing side is inhibited by the Coriolis force. Under heated thermal boundary conditions, the vortex pair near the trailing side reappears due to the effect of buoyancy force. These results indicate that the buoyancy force has a substantial effect on the secondary flow regime under thermal boundary conditions.

Keywords: flow dynamic, rotating smooth channel, secondary flow, buoyancy force

1. Introduction

It is widely believed that the turbine inlet temperature has a substantial effect on the efficiency of aero-engines. Thus, turbine blades must be operated in environments with extremely high temperatures. However, the gas temperature of the turbine inlet is far beyond the melting point of any material. To avoid this obstacle, many cooling technologies have been invented to protect gas turbines. Internal cooling is one of the most classical methods used to maintain an appropriate temperature for gas turbines. Over the past several years, a vast number of studies dealing with internal cooling have been reviewed by Han and Huh [2, 3]. However, the research

Received: Mar 05, 2019 AE: ZHANG Hongwu Corresponding author: YOU Ruquan E-mail: youruquan10353@buaa.edu.cn

Nomenclature

AR	aspect ratio	Z	Z-axis direction
D	hydraulic diameter/m	**Greek symbols**	
$\boldsymbol{f}$	force vector/N	Γ	circulation
$\boldsymbol{g}$	acceleration of gravity/m·s^{-2}	γ	volumetric expansion coefficient
i	unit vector of X-direction	μ	dynamic viscosity/N·s·m^{-2}
j	unit vector of Y-direction	ρ	density of the coolant/kg·m^{-3}
k	thermal conductivity/W·(m·K)$^{-1}$	σ	change of relative density
M	magnification factor/pixel·mm^{-1}	Ω	rotating speed/r·min^{-1}
q	heat flux/W·m^{-2}	$\boldsymbol{\Omega}$	rotating speed vector/ r·min^{-1}
Ro	rotation number	**Subscripts**	
r	radius/m	bCen	buoyancy force induced by centrifugal force
T	temperature/K	bCor	buoyancy force induced by the Coriolis force
U	velocity/m·s^{-1}	Cor	Coriolis
$\boldsymbol{U}$	velocity vector/m·s^{-1}	e	exterior
v	component of the velocity vector's size/m·s^{-1}	w	wall
X	X-axis direction	x	component of X-axis direction
Y	Y-axis direction	y	component of Y-axis direction

in this paper focuses on the middle section of the blade, which has systems of serpentine cooling passages. Researchers always simplify these cooling passages as rotating U-shaped channels or straight radial outlet channels to reduce the difficulty of the experiment. However, a secondary flow will clearly appear in a channel that is rotating. Research on secondary flow can help us better understand the flow and heat transfer mechanisms. Therefore, in this paper, we mainly study the secondary flow in a straight, smooth rotating channel with a square cross-section.

Experimental studies of secondary flow features in smooth rotating channels have been limited in the past by rotating test technology; proper rotating test technologies have only been developed in recent years. Based on the characteristics of the current work, the introduction will be divided into two branches: secondary flow research without thermal boundary conditions, which only considers the Coriolis force, and secondary flow research with thermal boundary conditions, which considers both the buoyancy force and Coriolis force.

1.1 Effect of the Coriolis force on secondary flow

In 1971, Hart [4] became the first to study secondary flow with an experimental and numerical analysis. The authors of this seminal work studied the secondary flow stability of fully developed laminar flow in a smooth channel (ratio of the channel width to channel height, AR=8). Moreover, they proposed that when the Reynolds number Re is known, the vortex regime relates to the rotation number Ro. When the rotation number is less than a critical number, the secondary flow state exhibits a pair of symmetrical vortices. If the rotation number exceeds this value, there will be a series of small vortices on the leading side. As the rotation number continues to increase, the fluid in the channel enters the "Taylor-Proudman state", which means that the gradient of the primary velocity profile in the core region is 0, and the vortices at the leading side disappear.

In 1982, Speziale and Thangam [5] studied the secondary flow of fully developed laminar flow in a smooth channel (AR=2) with a numerical method. The paper stated that when Ro<0.01, there will be a pair of symmetric vortices in the channel due to the Coriolis force. When 0.01<Ro<1, the vortex pair becomes stronger. When Ro>1, the symmetric vortex pair disappears and a four-vortex regime appears instead. Moreover, these authors also repeated the work of Hart et al. [4] and obtained the same results.

Smirnov and Yurkin [6] studied a flow visualisation experiment in a rotating channel (AR=1), and they discovered nine flow regime boundaries. Kheshgi and Scriven [7] studied the fully developed flow in a rotating smooth channel in 1985 using a numerical method. They found that the two-vortex regime is not stable for secondary flow under low rotational speed and that it is easy to form a four-vortex regime. For high rotational speed conditions, a stable two-vortex regime can be formed. In addition, the conversion process of the two structures exhibits a bifurcation phenomenon, which means that one Ro number can correspond to a two-vortex regime or a four-vortex regime. Based on

these studies, Nandakumar and Raszillier [8] studied the same problems in 1991. They also found that the secondary flow regime exhibits the bifurcation phenomenon for fully developed flow in a rotating smooth channel. In addition, they obtained the relationship that explains how the secondary flow and primary flow can affect each other. For the four-vortex regime, the primary velocity profile of the trailing side will induce a severe velocity defect. For the two-vortex regime, the primary velocity profile of the trailing side is very broad. Iacovides and Launder [9] investigated the fully developed turbulent flow and heat transfer in a rotating channel with a numerical simulation. A vortex pair in the cross-section plane was discovered near the trailing wall.

In addition to the abovementioned studies, Macfarlane, Joubert and Nickels [10, 11] and Watmuff, Witt and Joubert [12] used a hot-wire anemometer to measure the secondary flow field in a rotating channel. Macfarlane, Joubert and T. B. Nickels [10, 11] studied the effect of *AR* on the secondary flow, where *AR*=1:4, 1:2, and 1:1. It is important to note that most of the results obtained the four-vortex regime. When *AR*=1:1 and the parameters are same, the results are in good agreement with the current work. Watmuff, Witt, and Joubert [12] discovered a series of vortices at the trailing side, which were not present at the leading side.

Particle Image velocimetry (PIV) techniques have been developed in recent years, and researchers have gradually applied these techniques to investigate secondary flow regimes. Elfert et al. [13–15] measured the secondary flow regime in an irregular rotating cross-section; they found that the secondary flow regime is very complex due to the close connection of the secondary flow regime with the cross-section shape of the channel. Xie et al. [16] studied the flow structure and heat transfer in a square channel with different rib shapes. Their results showed that the use of downstream ribs is a suitable way to decrease the pressure loss and improve the flow structure, while maintaining a comparable enhancement in heat transfer, as expected.

Yao et al. [17, 18] investigated turbulent flow through a straight square duct by numerical simulation. They found that turbulence-driven secondary motions that arise in duct flows act to transfer fluid momentum from the centre of the duct to its corners. Wang et al. [19] investigated the heat transfer and fluid flow in a rotating rectangular channel with discrete ribs of various shapes by numerical simulation (*AR*=2:1); they found that a small streamwise rib can effectively enhance the heat transfer of the leading side. The heat transfer decreases gradually as the size of the streamwise rib increases.

Wei et al. [1] used PIV techniques to investigate the interaction between the primary flow fields and the secondary flow fields in a rotating smooth channel (*AR*=1). They discovered a series of vortices near the trailing side, and a pair of vortices appears at the leading side close to Ekman layer. At the core region of the flow field, a source point appears.

1.2 Effect of the buoyancy force on secondary flow

The buoyancy force is taken into account because of the addition of thermal boundary conditions. However, the addition of thermal boundary conditions can better approximate real aero-engine operating conditions. The first study to include these boundary conditions was not carried out until 1990. In recent years, Mayo et al. [20–22] used Time-resolved Particle Image Velocimetry (TR-PIV) to investigate the features of flow in a rotating channel with the effect of buoyancy force; they found that the buoyancy force has a substantial effect on the leading side and that it stabilises the vortices close to the leading side. Li et al. [23, 24] investigated the heat transfer in a rotating channel, and they found that the Coriolis force and buoyancy force both have a substantial effect on the leading and trailing sides.

You, Li, Xu et al. [25–27] used PIV techniques to measure the two-dimensional heat transfer, primary flow and secondary flow in a rotating smooth channel under a thermal boundary condition. In the same streamwise position, they discovered a pair of vortices at the cross-section that were induced by the Coriolis force; as the *Ro* increased, the vortex pair moved to the trailing side. Along with the streamwise position, the vortex pair also moved to the trailing side. When the *Ro* continued to increase, the regime of the secondary flow changed from a vortex pair regime to a four-vortex regime, as two small vortices appeared near the leading side.

However, there are few studies on secondary flow in a rotating channel under heating conditions. Our previous work [1] conducted experiments without thermal boundary conditions. Therefore, in this current work, we conduct the experiment with and without a constant heat flux thermal boundary condition, and then we compare their results. The leading side and the trailing side are heated under a constant heat flux q_w=380 W/m^2. The Reynolds number *Re* equals 4750, the *Ro* ranges from 0 to 0.26, and the streamwise positions are divided into three zones, as in our previous work. This will give us a deeper understanding of the secondary flow and heat transfer mechanism in the rotating smooth channel with thermal boundary station.

2. Apparatus and Measurement Procedure

2.1 Rotating facility

The experimental apparatus is shown in Fig. 1, which consists of a 1-m-diameter disc that rotates around a vertical shaft; the test sections and data acquisition

devices are all mounted on the disc. The rotating apparatus is driven by a DC motor through a belt drive, and the rotational speed is controlled by a digital converter (Eurotherm SSD 590). In addition, a high precision encoder (Ren-ishaw Tonic T2000) is installed on the rotating shaft to ensure the accuracy of the rotational speed measurement and the trigger position; further details will be given below.

The coolant air is provided by a blower (RHG-520). First, it mixes with the seeding particles (di-ethyl-hexyl-sebacate) to ensure uniform mixing. Then, the mixture enters into a float type flow meter. Next, the mixture should pass through a settling chamber (Screen & Honeycomb) to smooth it before entering the test section. The entrance turbulence intensity can be reduced to less than 1% [28]. More details about this are shown in Fig. 2.

A balance weight is installed on the opposite side of the disc to ensure the balance of both sides. Owing to the good balance of the rotating disc, the whole facility experiences very little vibration. On the other hand, the balance weight ensures the uniformity of the coolant air. Thermocouples are used to measure the temperature of the heated walls, inlet air temperature and air temperature before the float type flow meter. The analogue signals are converted to digital signals before passing the signal slip rings, which is used to convert the rotating signals to non-rotating signals. The coolant air pressure before the flow meter is measured by a pressure sensor. All of these analogue signals are transmitted to digital signals by the ADAM modules and then sent to a computer. In the current work, a CCD camera and laser are placed outside of the rotating facility, and the CCD camera and laser are simultaneously triggered by a high accuracy field-programmable gate array (FPGA) module. The walls are heated by a stabilised power source (DWW-K type) that can apply heat under constant voltage or constant current. The maximum power of the power source can reach 600 V × 5 A.

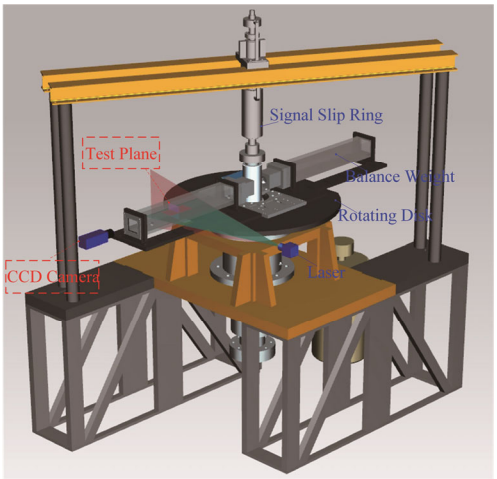

Fig. 1 Rotating facility

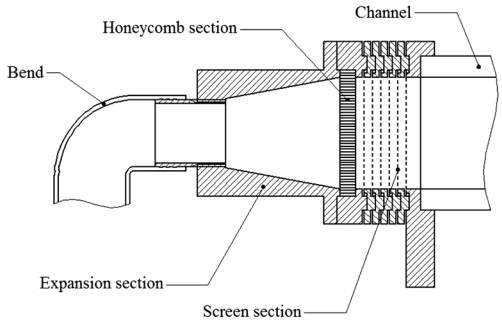

Fig. 2 Settling chamber

2.2 Test section

Fig. 3 shows a schematic diagram of the current test channel, which consists of the coordinate system, the leading and trailing walls, and an array of test sections. Table 1 shows the experimental conditions. The test section is 720 mm in length; the cross-section (internal size) is 80 mm × 80 mm, and the distance between the entrance and the centre of the rotating shaft is 211 mm. The measurements are made in the planes located at X=445 mm, 525 mm, and 605 mm, which are named Plane 1, Plane 2, and Plane 3, respectively. The square cross-section channel consists of four 15-mm-thick pieces of Plexiglas, which are formed together to create the whole channel. Table 1 shows the experimental parameters used for PIV acquisition. Table 2 shows the magnification factors on different planes.

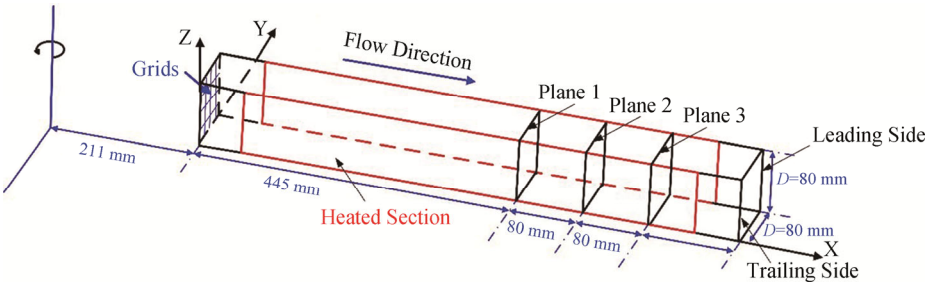

Fig. 3 Test section

Table 1 Experimental parameters

Re	*Ro*	Image pairs	Delay time/μs	Thermal boundary conditions
4750	0, 0.13, 0.26	500	30	With heat flux
4750	0, 0.13, 0.26	500	30	Without heat flux

Table 2 Magnification factors in the different planes

Plane	1	2	3
Magnification factor/ pixel·mm^{-1}	17.3750	19.2502	21.7502

There is a 1-mm-thick indium-tin-oxide (ITO) glass heater applied to each of the internal walls. According to the manufacturer, the ITO glass heaters have a thin conductive film of only 135 nm (±4%), and the light transmittance can reach 84% at the visible wavelength. This film can provide a uniform heat flux across the channel, which ensures the reliability of our experimental data. Owing to the film, the ITO glass can be heated to 300°C. However, in the current work, the leading side and trailing side are heated to approximately 50°C, which is far from the temperature limit. Therefore, there are no obvious differences in light transmittance, and the resistance changes are within 1%. To enhance the uniformity of the electrical conduction, there is a length of conductive tape on each side of the ITO glass heaters. To prevent heat loss on the channel side, a 10-mm-thick Plexiglas chamber is used as a heat insulation material to reduce heat loss.

In the current work, the Reynolds number is taken as 4750, and the rotation numbers range from 0 to 0.26. The thermal boundary conditions are taken into account: the leading side is heated under a constant heat flux q_w=380 W/m^2 which is calculated by the total energy generated by the ITO glass (q_{total}) minus the heat dissipates into the environment (q_{loss}). The top and bottom walls are not heated and are isothermal at room temperature.

2.3 PIV measurement

PIV measurement is an advanced optical measurement technique whose most important feature is its non-contact measurement approach; this type of measurement does not affect the internal flow field or heat transfer. By the simultaneous triggering of the CCD camera and lasers, the flow field can be accurately measured.

In the current work, the lasers are generated by a dual-cavity 135 MJ Nd:YAG pulse laser (532 nm) and guided via a light-guiding arm to the test plane with a thickness of approximately 1 mm. The CCD camera (2048 pixel × 2048 pixel, 14 bits, 14.7 fps) with a Nikon macro lens (105 mm) takes the photos and then transfers them to the computer. The particle is generated by a Laskin-nozzle-based seeding particle generator whose working particle is DEHS, as mentioned above.

Our previous work [1] has proven that 500 image pairs can ensure that the time-averaged velocities are statistically converged. Thus, in each condition, we capture 500 image pairs to satisfy the convergence condition. In the current work, the CCD camera and laser are simultaneously triggered. A FPGA-based trigger signal generator is used as an external fixed-point trigger. When the rotating disc rotates to a set position, the CCD camera and laser work simultaneously. In this way, we can obtain 500 image pairs.

The Flow-Master software is used to process the image pairs. Due to the time delay of the image pairs and the rotational speed, a movement between the image pairs appears which induces a much larger seeding particle displacement than the true movement, which is approximately 25% of the interrogation region dimensions. This phenomenon can induce spurious correlations between image pairs. Therefore, an initial window shift is used first to correct the experiment so that the seeding particles can move approximately 8 pixel to 10 pixel; this is considered to be the best approach. The flow field is calculated with the two-pass PIV interrogation algorithm. First, the image pairs are divided into a number of interrogation regions whose dimensions are 64 pixel × 64 pixel, and then the images are analysed to obtain a preliminary velocity field. Second, the dimensions of the interrogation region are changed to 32 pixel × 32 pixel, and the images are analysed again to obtain a more accurate velocity field. Once a velocity vector field is calculated, vector validation algorithms must be applied to eliminate the spurious correlations. In the current work, the peak ratio value is used as a post-processing criterion for eliminating false vectors, and the peak ratio value is 1.5.

3. Uncertainty Analysis

3.1 Uncertainty of PIV

The measurement errors of PIV contain bias errors and random errors. The sources of bias errors mainly include peak-locking, in-plane loss of correlation, out-of- plane loss of correlation, and the error caused by the velocity gradient in the interrogation regions.

The sources of random errors mainly include the displacement of the seeding particles, the size of the interrogation regions, the diameter of the seeding particles, the density of the seeding particles, the distribution of the laser intensity, the focusing quality of the images, the circuit noise of the CCD, the temperature uniformity of the heated walls, etc.

We utilise some techniques to reduce the effect of the bias errors. The peak-locking phenomenon is mainly due to the diameter of the seeding particles being too small (less than 1 pixel). To avoid this effect, we control the diameter of the seeding particles (2 to 4 pixels) in the current work. Out-of-plane loss of correlation is mainly due to the flow perpendicular to the laser light sheet. We control the exposure delay time to approximately 30 μs. However, the other two bias errors are reduced by the inline algorithm of the Flow-Master software.

For random errors, in the current work, we conduct the experiment with static PIV and precise phase-locking techniques. The fundamental theory of PIV techniques is as follows:

$$u = M\frac{\Delta s}{\Delta t} \tag{1}$$

here M is the magnification factor obtained at calibration and Δt is the time interval of the two pieces of laser triggered by the measurement system and controlled by us. Δs is the displacement of seeding particles in the two photos, u is the velocity value measured. Note that the errors of both of these terms can be neglected in this work. Therefore, the primary error comes from Δs. Under normal conditions, the image pairs are first divided into interrogation regions (32 pixel × 32 pixel in the current work). Then, we ensure that each interrogation region has 5 to 8 seeding particles. Moreover, we ensure that the displacement of the seeding particles is approximately equal to 1/4 of the interrogation region dimensions.

Following the experiment, we analysed our data to obtain the velocity error. The estimated uncertainty of the PIV measurements is 0.1 pixels following the approach outlined in Ref. [29]. With the delay time and the magnification factor of the measured planes, the relative measurement uncertainty (bias uncertainty [30]) for the secondary flow (approximately 0.25 m/s) in the core region can be seen in Table 3.

3.2 Uncertainty of hot-wire measurement

As the next chapter (Chapter 4.1) describes the results of the hot-wire measurement, some analysis of this is necessary. First of all, the calibration constitutes a major source of uncertainty. Streamline Pro Automatic Calibrator of Dantec is used to calibrate the hot-wire system. According to the user's manual, the uncertainty of the airflow velocity at the nozzle outlet is ±1%. As a 16 bit A/D converter is used to transfer the velocity data, the data acquisition related uncertainties can be neglected in the current work. Temperature variations during calibration will introduce systematic errors which should be corrected. In the current work, the uncertainty induced by temperature variations is ±1% after temperature correction. Considering all the error sources mentioned above, the uncertainty of the velocity measured with the hot-wire system is ±2.5%.

Table 3 Uncertainty of the secondary flow in different planes

Plane	1	2	3
Relative measurement uncertainty/m·s^{-1}	0.19	0.17	0.15

4. Results and Discussion

4.1 Data validation

To verify that the settling chamber can provide a uniform inlet velocity and to verify that the PIV data are reliable, the velocity profile is determined by hot-wire measurement and PIV measurement at the mid-span line (X=425 mm, Z=40 mm). The Reynolds number Re is equal to 15 000, and the rotation number Ro is equal to 0.

The data obtained by the hot-wire anemometer are compared with the PIV data, as shown in Fig. 4. A detailed description of the hot-wire technique can be seen in the work of Wei et al. [28]. The data obtained by the two measurements are in good agreement, which verifies the reliability of the PIV measurement in the current work.

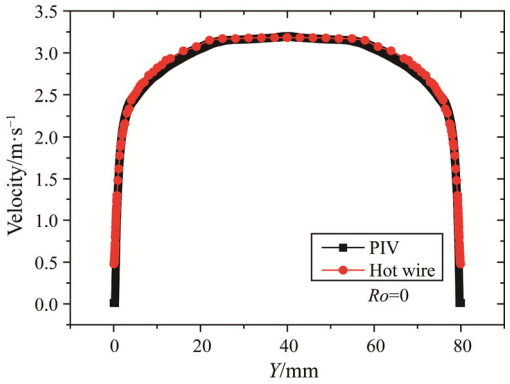

Fig. 4 Primary velocity profile at the mid-span line as measured by hot-wire and PIV methods

4.2 Effect of the thermal boundary conditions

Fig. 5 shows the secondary flow fields at Plane 2 with Re=4750 and Ro=0.13, which is the average result of 500 image pairs. This is also a typical secondary flow field for rotating smooth channels.

$$Re = \frac{\rho UD}{\mu} \tag{2}$$

$$Ro = \frac{\Omega D}{U} \tag{3}$$

here ρ is the density of the coolant; U is the average primary velocity of the inlet air flow; D is the hydraulic diameter of the channel; μ is the viscosity of the airflow, and Ω is the rotational speed. At least three obvious features can be detected from the secondary flow fields. First, a clear four-vortex flow field regime can be detected, which consists of a pair of vortices on the

trailing side and a pair of vortices on the leading side. Second, the peripheral velocity near the top-side and bottom-side, which is referred to as the Ekman layer, points towards the leading side, whereas the peripheral velocity in the core zone of the channel points towards the trailing side. Then, the peripheral velocity in the Ekman layer is greater than that in the flow core area; as the air flows towards the leading side, the high velocity region increases in thickness. To ascertain the reason for the above two features, we devised the following explanation.

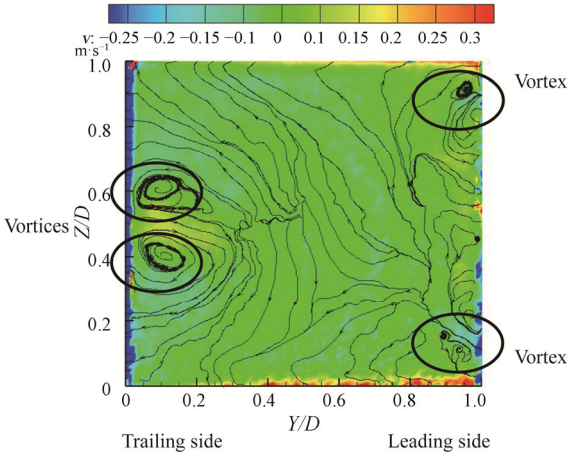

Fig. 5 Secondary flow fields at Plane 2 with *Re*=4750 and *Ro*=0.13

This result was first found by I. Macfarlane, Joubert P.N. and Nickels T.B. [10, 11] in 1998. They found that, in the smooth rotating channel (*AR*=1, which is the same as the current work), a pair of vortices appears at both the trailing side and the leading side, which is in good agreement with our current work. In the current work, the vortex pair of the trailing side is symmetrical near the wall. The vortex pair of the leading side is also symmetrical. However, the positions of the vortex pairs are different in the leading side, which have a vortex near the top and the bottom.

In addition, the flow near the Ekman layer points to the leading side. There are mainly two forces in the channel that can affect the flow (without heat): the Coriolis force and pressure gradient. When the Coriolis force is greater than the pressure gradient, the flow points to the trailing side, and vice versa. In the Ekman layer, the velocity of the fluid is much less than the primary velocity in the flow core area. Therefore, the Coriolis force is less than the pressure gradient, which points to the leading side.

$$\boldsymbol{f}_{\mathrm{Cor}} = -2 \cdot \rho \cdot \boldsymbol{\Omega} \times \boldsymbol{U} \tag{4}$$

here $\boldsymbol{U}$ is the primary velocity vector; $\boldsymbol{\Omega}$ is the rotation speed vector; $\boldsymbol{f}_{\mathrm{Cor}}$ is the Coriolis force vector. Thus, the flow direction near the Ekman layer points to the leading side. Then, the Coriolis force caused by the peripheral velocity points to the primary velocity. In turn, the fluid is accelerated and is constantly sucked into the Ekman layer, which causes the constant thickening of the high velocity region.

In the following section, we mainly discuss how the thermal boundary conditions affect the secondary flow. A constant heat flux is given by a stabilised power source (DWW-K type), and q_{w} is equals to 380 W/m^2.

$$q_{\mathrm{w}} = k \cdot \frac{\mathrm{d}T}{\mathrm{d}x} \tag{5}$$

here k is the thermal conductivity of the ITO glass heaters. Fig. 6(a)–(f) show the secondary flow states with and without heating at *Re*=4750 and *Ro*=0.13.

The results show that the secondary flow states are different under different thermal boundary conditions. One interesting conclusion that can be found from the secondary flow fields is that the vortex pair on the trailing side moves upwards from 5% to 12.5% of the hydraulic diameter when the airflow is heated by the stabilised power source. This phenomenon is due to the temperature of the leading and trailing walls being much higher than the air flow, which induces a density difference in the air. This density difference subsequently induces the buoyancy force, which can move the vortex pair upwards. Additional information about this phenomenon is shown in Table 4.

4.3 Effect of streamwise position

Figs. 7(a)–(c) show the secondary flow states along the streamwise position at *Re*=4750 and *Ro*=0.13. When the air flows downstream, there is a clear change in the vortex pair of the trailing side. Through the figures, we can detect that the downstream vortex (clockwise rotation) is smaller than the upstream vortex. The explanation for this phenomenon is given hereafter. First, it is common knowledge that the rotational coordinate system circulation dynamics equation is:

$$\frac{\mathrm{d}\Gamma}{\mathrm{d}t} = -\oint \left(2\boldsymbol{\Omega} \times \boldsymbol{U}\right) \cdot \delta \boldsymbol{r} + \oint \left(\sigma \boldsymbol{g}\right) \cdot \delta \boldsymbol{r} + \nu \oint \left(\nabla^2 \boldsymbol{U}\right) \cdot \delta \boldsymbol{r} \tag{6}$$

here σ is the change in relative density, which changes with the temperature difference between the wall and the air flow; $\boldsymbol{r}$ is the radial direction, $\boldsymbol{g}$ is the acceleration of gravity $\boldsymbol{v}$ is the secondary flow velocity. Moreover, the result of $\left(\nabla^2 \boldsymbol{U}\right) \cdot \delta \boldsymbol{r}$ is equal to 0. Thus, the final equation is as follows:

$$\frac{\mathrm{d}\Gamma}{\mathrm{d}t} = -\oint \left(2\boldsymbol{\Omega} \times \boldsymbol{U}\right) \cdot \delta \boldsymbol{r} + \oint \left(\sigma \boldsymbol{g}\right) \cdot \delta \boldsymbol{r} \tag{7}$$

To understand the abovementioned phenomenon, select the vortex pair of the trailing side and calculate the circulation. The schematic diagram of the integral path is shown in Fig. 8, wherein the red arrow represents the upside integral path; the blue arrow represents the downside integral path; the black arrow represents the

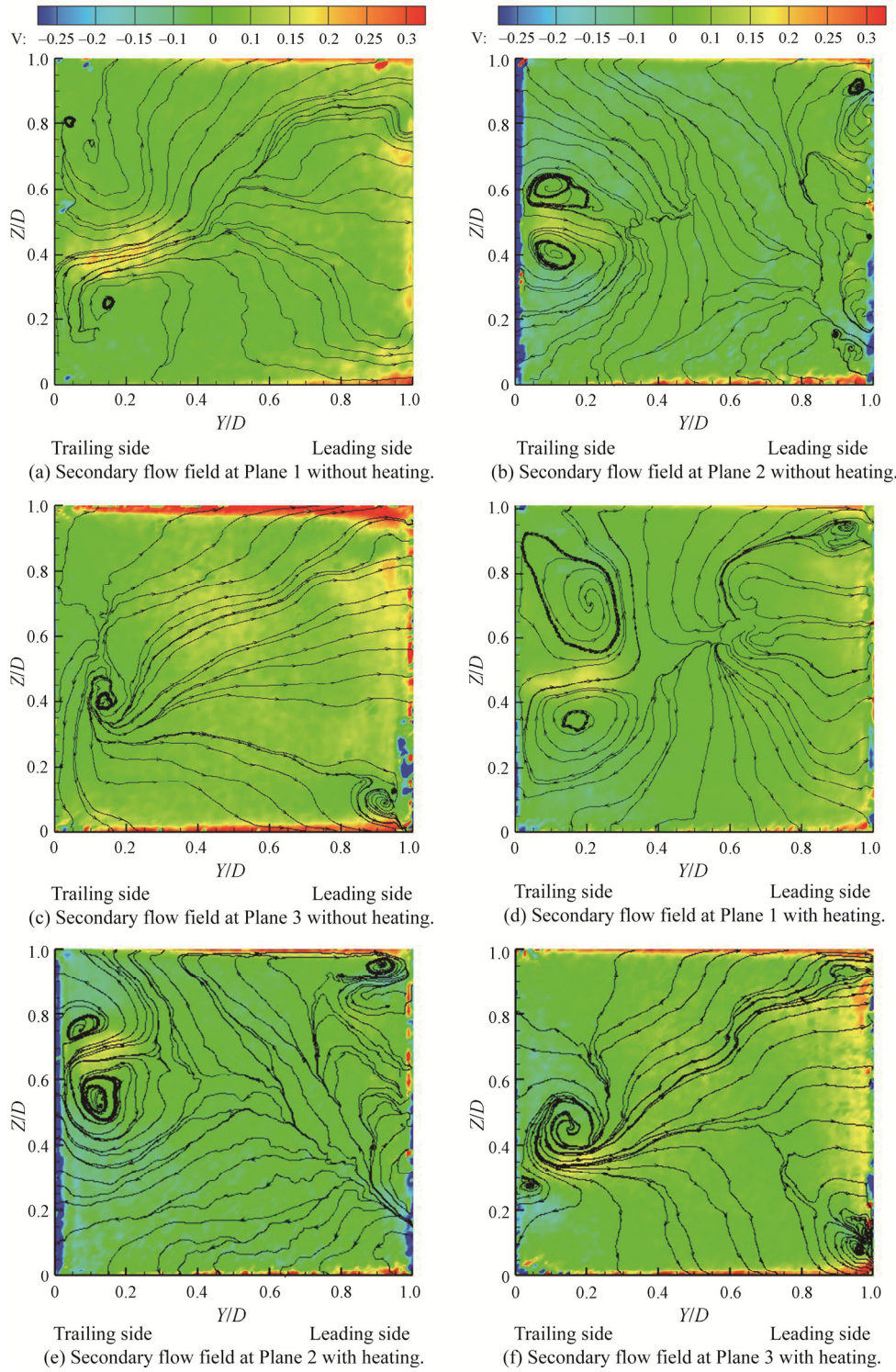

Fig. 6 Secondary flow field at the different planes with and without heating

Table 4 Relative change in vertical position of the vortex pairs

Plane	1	2	3
Relative change in vertical position	6.25%	12.5%	5%

rotational direction of the vortex; $\boldsymbol{U}_{\text{low}}$ represents the average primary velocity of Line 2, and $\boldsymbol{U}_{\text{high}}$ represents the average primary velocity of Lines 1 and 3. The specific derivation process will not be repeated; however, it can be found in Wei's work [1]. As such, only the results are presented here.

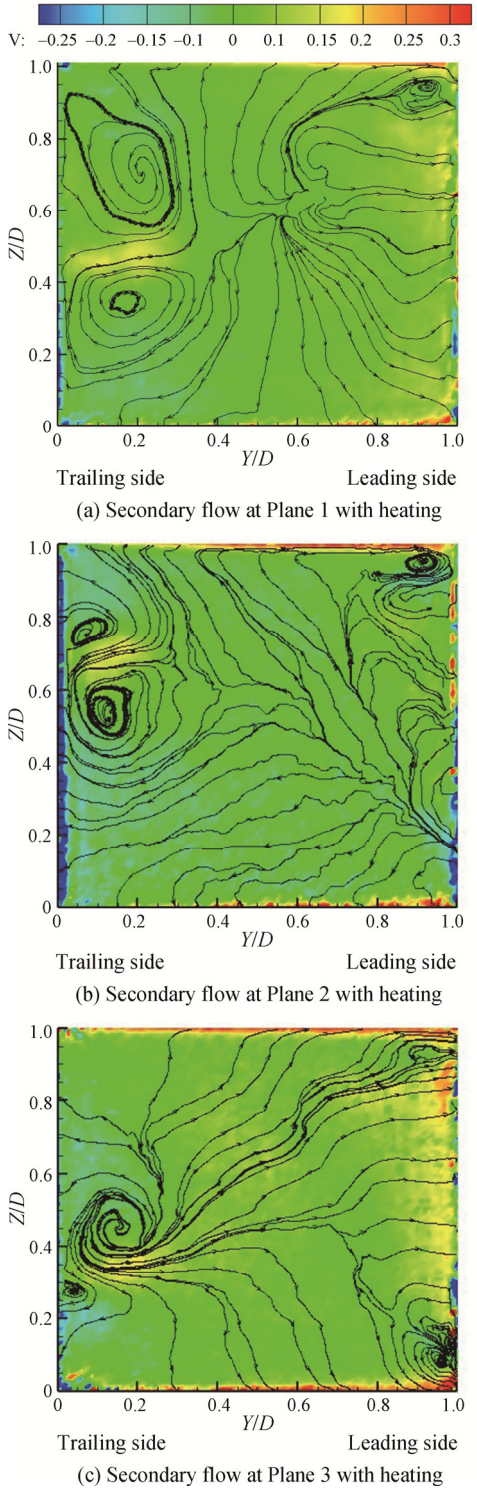

Fig. 7 Secondary flow at the different planes with heating

$$\frac{\mathrm{d}\Gamma_{\text{upside}}}{\mathrm{d}t}=2\left(\boldsymbol{U}_{\text{high}}-\boldsymbol{U}_{\text{low}}\right)\boldsymbol{\Omega}d+\oint(\sigma\boldsymbol{g})\cdot\delta\boldsymbol{r} \tag{8}$$

$$\frac{\mathrm{d}\Gamma_{\text{downside}}}{\mathrm{d}t}=2\left(\boldsymbol{U}_{\text{low}}-\boldsymbol{U}_{\text{high}}\right)\boldsymbol{\Omega}d+\oint(\sigma\boldsymbol{g})\cdot\delta\boldsymbol{r} \tag{9}$$

We suppose that $\mathrm{d}\Gamma_{\text{vortex}}/\mathrm{d}t=\boldsymbol{U}_{\text{vortex}}\mathrm{d}\Gamma_{\text{vortex}}/\mathrm{d}x$, where $\boldsymbol{U}_{\text{vortex}}$ is the average primary velocity within the integral path. Thus, the final equation is as follows:

$$\Gamma_{\text{upside}}=\frac{2\left(\boldsymbol{U}_{\text{high}}-\boldsymbol{U}_{\text{low}}\right)\boldsymbol{\Omega}d}{\boldsymbol{U}_{\text{vortex}}}\left(x-x_0\right)+\left(x-x_0\right)\oint(\sigma\boldsymbol{g})\cdot\delta\boldsymbol{r} \tag{10}$$

$$\Gamma_{\text{downside}}=\frac{2\left(\boldsymbol{U}_{\text{low}}-\boldsymbol{U}_{\text{high}}\right)\boldsymbol{\Omega}d}{\boldsymbol{U}_{\text{vortex}}}\left(x-x_0\right)+\left(x-x_0\right)\oint(\sigma\boldsymbol{g})\cdot\delta\boldsymbol{r} \tag{11}$$

here x is the X-axis direction, $(\boldsymbol{U}_{\text{high}}-\boldsymbol{U}_{\text{low}})>0$, and $(\boldsymbol{U}_{\text{low}}-\boldsymbol{U}_{\text{high}})\,\boldsymbol{\Omega}d<0$. According to the derivation results, if the term $\left(x-x_0\right)\oint(\sigma\boldsymbol{g})\cdot\delta\boldsymbol{r}$ does not exist, Γ_{upside} will become stronger along the streamwise direction, whereas Γ_{downside} will become weaker. This result is in good agreement with the current experimental results.

However, this term does exist now, it can be concluded that the value of $\left(x-x_0\right)\oint(\sigma\boldsymbol{g})\cdot\delta\boldsymbol{r}$ cannot make an obvious impact on the equation under current heating condition. In other words, the primary influence factor is the circulation change induced by the Coriolis force.

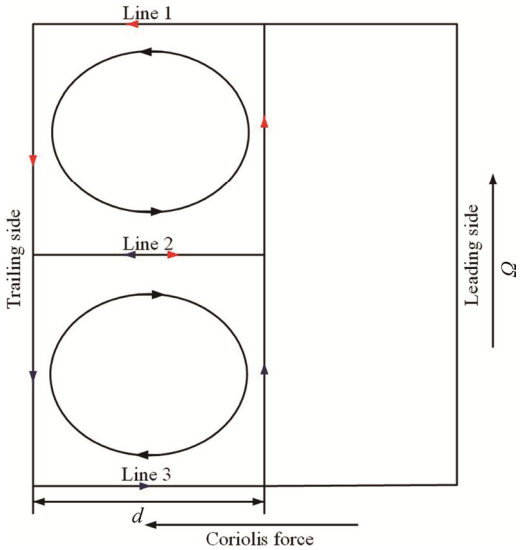

Fig. 8 Schematic diagram of the integral path

4.4 Effect of the rotation number

In this part, the effect of the rotation number will be taken into consideration. Fig. 9 shows the secondary flow state at Plane 2 when Ro=0.26 and Re=4750. There is a clear difference between the heated and unheated conditions. The vortex pair of the trailing side appears again under heated conditions; however, the vortex pair disappears under unheated conditions. The explanation for this phenomenon is presented hereafter.

It is common knowledge that if heating conditions are considered, it is necessary to consider both the Coriolis force and the buoyancy force. The buoyancy force is related to the Coriolis force, centrifugal force and temperature field. The equation of buoyancy force is given below.

$$\boldsymbol{f}_{\mathrm{b}} = -\rho\gamma\boldsymbol{\Omega}\Delta T\left(-2v_x\boldsymbol{j} + \Omega r\boldsymbol{i}\right) \tag{12}$$

$$\gamma = -\frac{1}{\rho}\left(\frac{\partial\rho}{\partial T}\right)_p \approx \frac{1}{T} \tag{13}$$

$$\Delta T = T - T_0 \tag{14}$$

here $\boldsymbol{f}_{\mathrm{b}}$ is the buoyancy force; ρ is the density under the reference temperature T_0; T_0 is the average temperature of the whole cross-section; γ is the volumetric expansion coefficient of the airflow, which can be regarded as $1/T$ in the current work; and v_x is the X-axis component of the velocity vector. As shown in the equations above, $\boldsymbol{f}_{\mathrm{b}}$ contains two parts: the buoyancy force induced by the centrifugal force and the buoyancy force induced by the Coriolis force. The explanation will be given below, and the schematic diagrams are shown in Fig. 10. First, the buoyancy force induced by centrifugal force is:

$$\boldsymbol{f}_{\mathrm{bCen}} = -\rho\gamma\boldsymbol{\Omega}^2\Delta Tr\boldsymbol{i} \tag{15}$$

The direction of this component of the buoyancy force is the X-axis (positive direction or negative direction); in the current work, this component will not be considered because we are discussing the secondary flow.

The buoyancy force induced by the Coriolis force is given by the following equation:

$$\boldsymbol{f}_{\mathrm{bCor}} = 2\rho\gamma\boldsymbol{\Omega}\Delta Tv_x\boldsymbol{j} \tag{16}$$

Obviously, v_x is greater than zero because there is no backflow. For the air near the trailing wall, the direction of $\boldsymbol{f}_{\mathrm{bCor}}$ is positive up to the order of the Coriolis force.

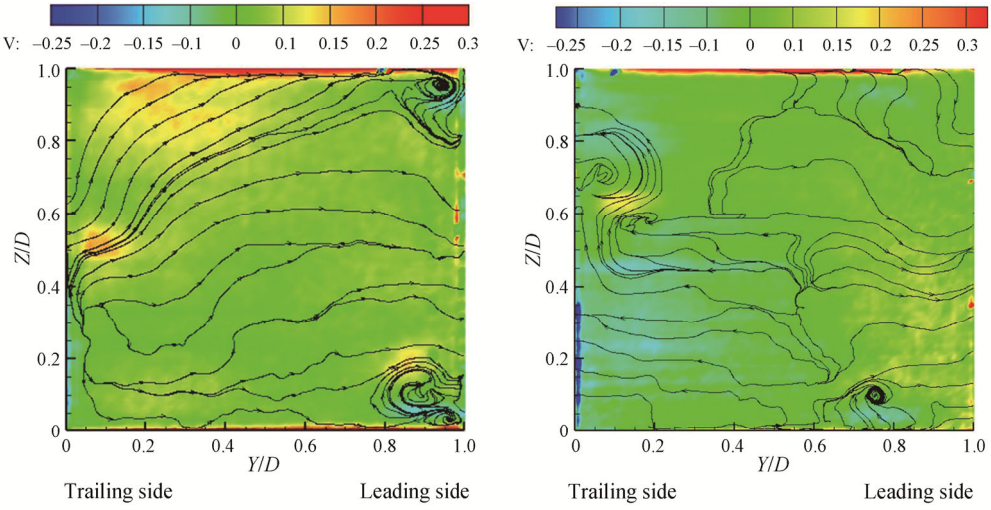

(a) Secondary flow at Plane 2 without heating (b) Secondary flow at Plane 2 with heating

Fig. 9 Secondary flow at Plane 2 with and without heating when Ro=0.26 and Re=4750

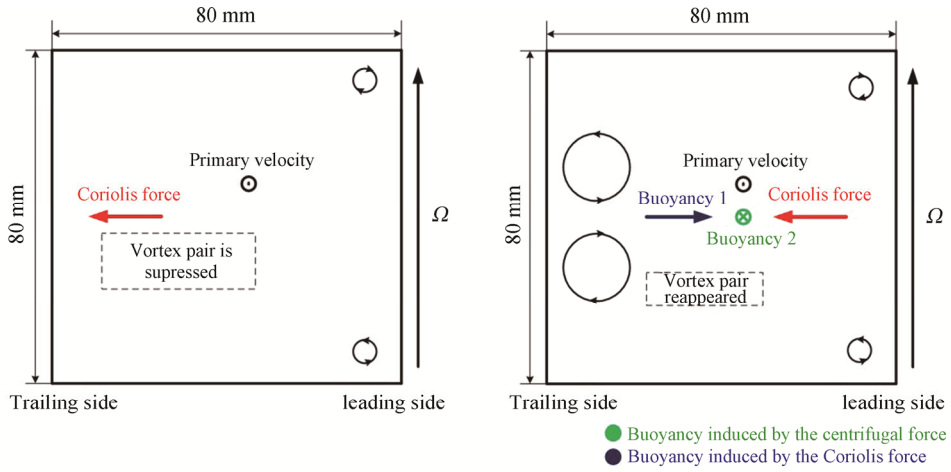

(a) Schematic diagram of the forces without heating (b) Schematic diagram of the forces with heating

Fig. 10 Schematic diagram of the forces

According to the experimental results, the value of f_{bCor}/f_{Cor} is approximately 19.5%, and the two forces restrict each other. Therefore, the vortex pair of the trailing side suppressed by the Coriolis force reappears.

5. Conclusion

An experimental study was conducted in a smooth rotating channel under a thermal boundary condition, and the results were compared to those of the same channel without heating. The experiment was performed with Re=4750 and Ro ranging from 0 to 0.26. The secondary flow field was obtained by PIV techniques to explain how the thermal boundary conditions can affect the secondary flow fields. According to the results, the main conclusions are summarised as follows.

(1) The buoyancy force induced by the Coriolis force and centrifugal force can substantially affect the secondary flow regime.

(2) A four-vortex regime is detected in the current work, which includes a pair of symmetric vortices at both the trailing side and the leading side. The peripheral velocities that are near the top-side and bottom-side and referred to as the Ekman layer, point towards the leading side, whereas the peripheral velocity in the core zone of the channel points towards the trailing side. The peripheral velocity in the Ekman layer is greater than the velocity in the flow core area. As the air flows towards the leading side, the thickness of the high velocity region is increased.

(3) Due to the heating of the leading side and the trailing side, the buoyancy force causes the vortex pair of the trailing side to rise along the Z-axis.

(4) The vortex pair of the trailing side changes substantially in the streamwise direction. When moving upstream along the streamwise direction, the upper vortex near the trailing wall becomes weaker, whereas the lower vortex becomes stronger; this phenomenon can be explained by theoretical analysis. Therefore, it is obvious that the change in relative density cannot make a substantial difference compared to that of the Coriolis force. Therefore, the intensity of the vortex is still controlled by the Coriolis force.

(5) Due to the increasing rotational speed, the Coriolis force, which points to the trailing side, also increases. The Coriolis force causes the vortex pair of the trailing side to disappear. However, when the leading side and the trailing side are heated, the vortex pair reappears. This is because the direction of the buoyancy force induced by the Coriolis force acts in the opposite direction of the Coriolis force.

Acknowledgement

The present work is financially supported by the National Natural Science Foundation of China (No. 51822602) and the Fundamental Research Funds for the Central Universities (No. YWF-19-BJ-J-293).

References

[1] Wei K., Tao Z., Wu H., et al., Interaction between the primary flow fields and the secondary flow fields under rotating condition. Experimental Thermal and Fluid Science, 2017, 84: 217–230.

[2] Han J.C., Huh M., Recent studies in turbine blade internal cooling. Heat Transfer Research, 2009, 41(8): 803–828.

[3] Han J.C., Recent studies in turbine blade cooling. International Journal of Rotating Machinery, 2004, 10(6): 443–457.

[4] Hart J.E., Instability and secondary motion in a rotating channel flow. Journal of Fluid Mechanics, 1971, 45(2): 341–351.

[5] Speziale C.G., Thangam S., Numerical study of secondary flows and roll-cell instabilities in rotating channel flow. Journal of Fluid Mechanics, 1983, 130(1): 377–395.

[6] Smirnov E.M., Yurkin S.V., Fluid flow in a rotating channel of square section. Fluid Dynamics, 1983, 18(6): 850–855.

[7] Kheshgi H.S., Scriven L.E., Viscous flow through a rotating square channel. Physics of Fluids, 1985, 28(10): 2968–2979.

[8] Nandakumar K., Raszillier H., Durst F., Flow through rotating rectangular ducts. Physics of Fluids, 1991, 3(5): 770–781.

[9] Iacovides H., Launder B.E., Parametric and numerical study of fully-developed flow and heat transfer in rotating rectangular ducts. Journal of Turbomachinery. 1991, 113(3): 331–338.

[10] Macfarlane I., Joubert P.N., Effects of secondary flows on developing, turbulent, rotating boundary layers. Experimental Thermal and Fluid Science, 1998, 17(1–2): 79–89.

[11] Macfarlane I., Joubert P.N., Nickels T.B., Secondary flows and developing, turbulent boundary layers in a rotating duct. Journal of Fluid Mechanics, 1998, 373(373): 1–32.

[12] Watmuff J.H., Witt H.T., Joubert P.N., Developing turbulent boundary layers with system rotation. Journal of Fluid Mechanics, 1985, 157: 405–448.

[13] Elfert M., Schroll M., Förster W., PIV measurement of secondary flow in a rotating two-pass cooling system with an improved sequencer technique. ASME Turbo Expo: Power for Land, Sea, and Air, Glasgow, UK, 2010. DOI: 10.1115/GT2010-23510.

[14] Schroll M., Elfert M., Lange L., Investigation of the

Effect of Rotation on the Flow in a Two-Pass Cooling System with Smooth and Ribbed Walls using PIV. Asme Turbo Expo: Turbine Technical Conference and Exposition, Vancouver, Canada, 2011, 6: 1653–1664.

[15] Elfert M., Jarius M.P., Weigand B., Detailed flow investigation using PIV in a typical turbine cooling geometry with ribbed walls. ASME Turbo Expo: Turbine Technical Conference and Exposition, Lisbon, Portugal, 2004. DOI: 10.1115/GT2004-53566.

[16] Xie G., Zheng S., Zhang W., et al., A numerical study of flow structure and heat transfer in a square channel with ribs combined downstream half-size or same-size ribs. Applied Thermal Engineering, 2013, 61(2): 289–300.

[17] Yao J., Zhao Y., Fairweather M., Numerical simulation of turbulent flow through a straight square duct. Applied Thermal Engineering, 2015, 91: 800–811.

[18] Yao J., Zhou F., Zhao Y., et al., Investigation of erosion of stainless steel by two-phase jet impingement. Applied Thermal Engineering, 2015, 88: 353–362.

[19] Wang J., Liu J., Wang L., et al., Numerical investigation of heat transfer and fluid flow in a rotating rectangular channel with variously-shaped discrete ribs. Applied Thermal Engineering, 2018, 129: 1369–1381.

[20] Coletti F., Maurer T, Arts T., et al. Flow field investigation in rotating rib-roughened channel by means of particle image velocimetry. Experiments in Fluids, 2012, 52(4): 1043–1061.
DOI: 10.1007/s00348-011-1191-2.

[21] Coletti F., Jacono D.L., Cresci I., et al., Turbulent flow in rib-roughened channel under the effect of Coriolis and rotational buoyancy forces. Physics of Fluids, 2014, 26(4): 045111.

[22] Mayo I., Gori G.L., Lahalle A., et al., Aerothermal characterization of a rotating ribbed channel at engine representative conditions—Part I: high-resolution particle image velocimetry measurements. ASME Journal of Turbomachinery, 2016, 138(10): 101008.

[23] Li H., You R., Deng H., et al., Heat transfer investigation in a rotating U-turn smooth channel with irregular cross-section. International Journal of Heat and Mass Transfer, 2016, 96: 267–277.

[24] Li Y., Deng H., Tao Z., et al., Heat transfer characteristics in a rotating trailing edge internal cooling channel with two coolant inlets. International Journal of Heat and Mass Transfer, 2017, 105: 220–229.

[25] You R., Li H., Tao Z., Experimental investigation on two-dimensional heat transfer and secondary flow in a rotating smooth channel. International Journal of Heat and Mass Transfer, 2017, 113: 342–353.

[26] You R., Li H., Tao Z., et al., PIV measurements of turbulent flows in a smooth channel with the heated boundary under rotation conditions. Applied Thermal Engineering, 2017, 123: 1021–1033.

[27] You R., Li H., Wu H., et al., PIV flow measurements for a rotating square smooth channel heated by basically uniform heat flux, International Journal of Heat and Mass Transfer, 2018; 119: 236–246.

[28] Wei K., Tao Z., Deng H.W., et al., Interaction of secondary flow with developing, turbulent boundary layers in a rotating duct. ASME Turbo Expo: Turbine Technical Conference & Exposition, Montreal, Canada, 2015. DOI: 10.1115/GT2015-42828.

[29] Westerweel J., Theoretical analysis of the measurement precision in particle image velocimetry. Experiments in Fluids, 2000, 29(1): S003–S012.

[30] Coleman H. W., Steele W. G., Engineering application of experimental uncertainty analysis. AIAA Journal, 1995, 33(10): 1888–1896.